JOURNAL OF COMPUTATIONAL PHYSICS **110**, 11–22 (1994)

Simulation of Particle Trajectories in Bifurcating Tubes

IMRE BALÁSHÁZY

KFKI Atomic Energy Research Institute, Health Physics Department, P.O. Box 49, H-1525 Budapest 114, Hungary

Received October 11, 1991; revised March 9, 1993

A numerical method for computing aerosol particle trajectories in bifurcating tubes has been elaborated. The model consists of three characteristic parts: (i) construction of the geometry of the bifurcation, (ii) calculation of the fluid flow field, and (iii) computation of the particle trajectories. The geometry was designed on a three-dimensional computer mesh. The flow field was formulated by solving the steady-state Navier–Stokes and Poisson equations with a finite difference approximation. The particle trajectories were generated having assumed the simultaneous action of inertial impaction, gravitational sedimentation, Brownian motion, and interception mechanisms. With a knowledge of particle trajectories one can examine the spatial distribution of deposition or the penetration efficiencies of particles in bifurcations. In this paper only the model is detailed; its usage in examining aerosol particle deposition in airway bifurcations is presented elsewhere for both inhalation and exhalation. © 1994 Academic Press, Inc.

1. INTRODUCTION

The behavior of aerosol particles or that of a particulate suspension in a liquid (lyosol) in bifurcating tubes is important in several fields of science and engineering, e.g., deposition of inhaled particles in the lung, the movement of blood clots in veins, determination of deposition efficiencies of ambient air or water samplers, penetration of radioactive aerosols in the various ducts of nuclear power plants, penetration of aerosols in ventilation systems in mining or other industrial establishments.

A number of analytical and numerical methods have been worked out to characterize the motion of aerosols and lyosols in straight or bent tubes. However, despite the great importance of the topic there is no appropriate model for describing particle behavior in bifurcations. In virtually every case bifurcations are modeled by bent or straight tubes. We know of only a few exceptions: (i) that in which the local deposition fluxes of aerosol particles in a symmetrical tracheobronchial tree bifurcation are calculated having supposed inertial impaction and diffusion deposition mechanisms [17]. However, in [17] the effect of gravitation is not taken into account; moreover, the impaction mechanism assumptions are not sufficiently accurate for the submicron particles they are treating (for more details see Section 4); (ii) two-dimensional models are detailed in [10, 11, 35]; (iii) a numerical model for particle deposition in bifurcating tubes was outlined in [30], but—so far as I am aware—no details have ever been elaborated; (iv) in [14] a two-dimensional model computes the air flow only and not the trajectories of particles; (v) the model in [26] considers tubes of rectangular cross section, and impaction and gravitation are considered only when computing particle motion.

Here a numerical model is given for calculating trajectories and deposition sites of spherical particles in a symmetrical or asymmetrical tube bifurcation with either a narrow or wide bifurcation region. Since the fluid is assumed to be incompressible the model can be applied only for subsonic gas velocities in which the relative pressure drop is small. Here we would mention that in human airways the pressure differences are very small and the pressure varies as much within the cross section of an airway as it does across a junction [20, 29]. Moreover, we assume laminar flow and employ the steady-state Navier–Stokes equations. It is worth noting here that in [34] the authors measured the formation of the flow field in bifurcations in analogy with the airways in humans and they found no turbulence; they did, however, find strong asymmetry in the flow at the carinal ridge and effective secondary flows in the daughter airways for inhalation. Despite this, the fact that we assume laminar steady-state flow means some limitations in the applicability of the model mainly at high flow rates (and Re numbers) in the upper airways.

2. CONSTRUCTION OF THE BIFURCATION GEOMETRY

A bifurcation is constructed from a parent branch and two daughter branches. It is a system in which three straight tube sections are joined together by a central zone. Because of the noncylindrical symmetry of the central part of the system the geometry of the bifurcation is generated in a Cartesian coordinate system by a cubic computer mesh. The bifurcation is characterized by eleven parameters: branch lengths L_{pA}, L_{pB}, L_{dA}, L_{dB}; branch diameters D_p, D_{dA}, D_{dB}; branching angles α_A, α_B; and two other angles β_A, β_B which are the angles between the respective daughter

0021-9991/94 $6.00

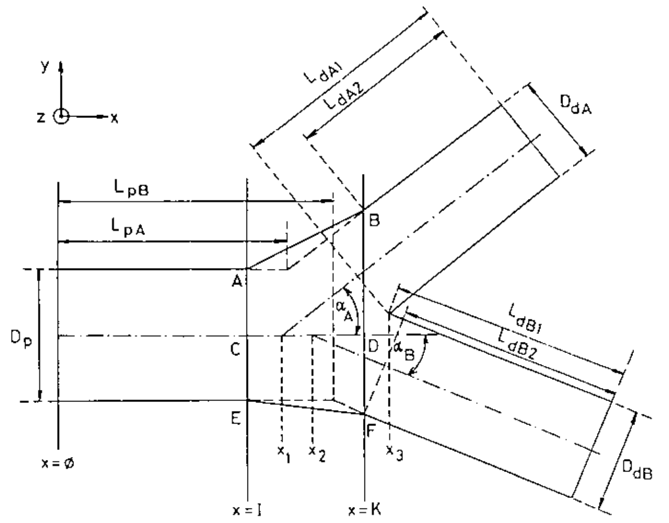

FIG. 1. Bifurcation geometry.

branches and the $z=0$ plane. Indexes p and d refer to the parent and daughter branches, and indexes A and B are related to the respective sides of daughters A and B. The value of coordinate y increases along daughter A and decreases along daughter B. (In some cases y is constant along the daughter branches.) The lengths of the daughters (L_{dA}, L_{dB}) are the arithmetic means of L_{dA1} and L_{dA2} or L_{dB1} and L_{dB2}, respectively (see Fig. 1). The axis of the parent airway is assumed to be parallel to the x-axis and the entrance of the parent tube lies in the $x=0$ plane. The position of the bifurcation in relation to gravity is optional.

A schematic projection of the bifurcation is shown in Fig. 1. The main relations between the parameters displayed in the figure are summarized as follows:

A. If neither of the branching angles is zero:

$$x_1 = L_{pA} + \frac{D_{dA} - D_p \cos\alpha_A}{2\sin\alpha_A}, \tag{1}$$

$$x_2 = L_{pB} + \frac{D_{dB} - D_p \cos\alpha_B}{2\sin\alpha_B}, \tag{2}$$

$$x_3 = \frac{\tan\alpha_A}{\tan\alpha_A + \tan\alpha_B}\left(L_{pA} + \frac{2D_{dA} - D_p\cos\alpha_A}{2\sin\alpha_A}\right) + \frac{\tan\alpha_B}{\tan\alpha_A + \tan\alpha_B}\left(L_{pB} + \frac{2D_{dB} - D_p\cos\alpha_B}{2\sin\alpha_B}\right). \tag{3}$$

Narrow and wide central parts of the bifurcation are defined in the following way:

(i) for a narrow bifurcation region the x coordinate of plane I in Fig. 1 is

$$I = L_{ps}, \tag{4}$$

where

$$L_{ps} = \min(L_{pA}, L_{pB}). \tag{5}$$

(ii) for a wide bifurcation region the x coordinate of plane I in Fig. 1 is

$$I = L_{pA} + L_{pB} - K, \tag{6}$$

where

$$K = \frac{x_3 + L_{pm}}{2} \tag{7}$$

and

$$L_{pm} = \max(L_{pA}, L_{pB}). \tag{8}$$

Because $K > x_3$ is considered to be an unrealistic shape, it is omitted from the analysis.

The parameters L_{dA1} and L_{dB1} are determined by the equations

$$L_{dA1} = L_{dA} + \frac{x_3 - L_{pA} - D_{dA}\sin\alpha_A}{2\cos\alpha_A}, \tag{9}$$

$$L_{dB1} = L_{dB} + \frac{x_3 - L_{pB} - D_{dB}\sin\alpha_B}{2\cos\alpha_B}; \tag{10}$$

in addition L_{dA2} and L_{dB2} are given by (9), (10), and the definitions of L_{dA} and L_{dB}, i.e., the lengths of the daughters, are the arithmetic means of L_{dA1} and L_{dA2} or L_{dB1} and L_{dB2}.

B. If one of the branching angles is zero, let $\alpha_A = 0$:

$$x_1 = -\infty, \tag{11}$$

x_2 is given by (2), and

$$x_3 = x_2 + \frac{D_{dB}}{2\sin\alpha_B} + \frac{2D_{dA} - D_p}{2\,\mathrm{tg}\,\alpha_B}. \tag{12}$$

In the case of monopodial branchings, $L_{pA} = L_{pB}$; thus

$$L_{dA1} = L_{dA} + \frac{x_3 - L_{pA}}{2}. \tag{13}$$

The geometry of the bifurcation is built up on a three-dimensional computer mesh of cubic elementary cells. The coordinates of the grid points were constructed on the basis of the equations which characterize the geometry of the bifurcation. The parent and the daughter branches are straight cylinders joined together by a central bifurcation zone whose superficies are generated by a smoothing func-

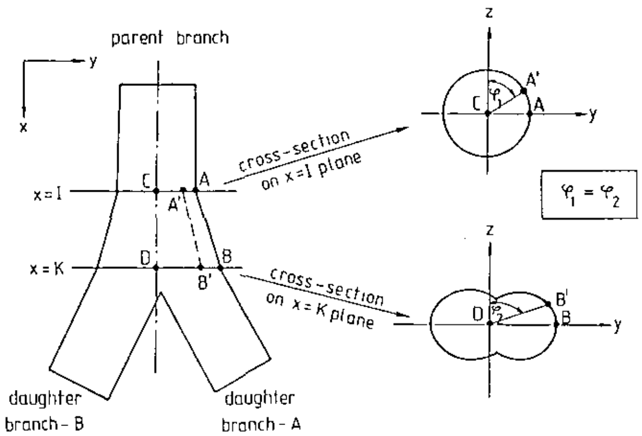

FIG. 2. Schematic illustration of construction of central bifurcation zone.

tion [19]. This central region is bordered by $x = I$ and $x = K$ planes and, in addition, by straight sections between these two planes connecting the surfaces of the parent and the daughter branches in such a way that the azimuthal angles on the $x = I$ and $x = K$ planes of these straight sections (φ_1 and φ_2 on Fig. 2) are identical to each other. The apexes of the angles of φ_1 and φ_2 are in a direct line with the axis of the parent branch (see Fig. 2).

The point in choosing both narrow and wide central bifurcation regions is that the width of this central part may significantly influence the fluid field in the vicinity of the carinal ridge and consequently may affect the trajectories and the accidental deposition of particles.

When generating the computer mesh a code number is assigned to each node point: first, in order to distinguish whether a given mesh point is in, on, or ouside—within less than the elementary grid cell distance—the coordinates of the bifurcation; second, to characterize to which part of the bifurcation the point belongs. In such a way the form of the generated computer mesh covers the required bifurcation and this code number is extremely useful for every part of the numerical analysis as a means of identifying the different sections of the bifurcation.

3. COMPUTATION OF THE FLUID VELOCITY FIELD

For determining the fluid flow field the Navier–Stokes equation (14) and the continuity equation (15) have been applied,

$$\frac{\partial \mathbf{v}}{\partial t} + (\mathbf{v} \cdot \nabla)\,\mathbf{v} = \mathbf{g} - \frac{1}{\rho}\nabla p + \frac{\mu}{\rho}\nabla^2 \mathbf{v} \tag{14}$$

and

$$\nabla \mathbf{v} = 0, \tag{15}$$

where $\mathbf{v}$ is the velocity of the fluid, $\mathbf{g}$ is the gravitational acceleration, p, ρ, and μ are the pressure, density, and viscosity of the fluid, respectively [12].

A finite difference approximation was utilized to solve (14) and (15), viz. the hybrid method of the stream function vorticity approach and the primitive variable approach [1]. The independent variables of this technique are the velocity and the vorticity of the fluid. Taking the rotation of (14), the pressure is eliminated and the result is [36]:

$$\frac{\partial \boldsymbol{\omega}}{\partial t} = \nabla \times (\mathbf{v} \times \boldsymbol{\omega}) + \nu \nabla^2 \boldsymbol{\omega}, \tag{16}$$

where $\boldsymbol{\omega} = \nabla \times \mathbf{v}$ is the vorticity, and ν is the kinetic viscosity of the fluid. With this method the vorticity is obtained from (16) and the velocity from the Poisson equation below:

$$\nabla^2 \mathbf{v} = -\nabla \times \boldsymbol{\omega}. \tag{17}$$

It is known (e.g., [2, 13, 31]) that the continuity equation, (15), is automatically satisfied by applying this method.

The course of the solution is the following: It begins with the determination of the initial conditions, i.e., with the specification of $\mathbf{v}$ and $\boldsymbol{\omega} = \nabla \times \mathbf{v}$ at each mesh point at $t = 0$. Then, as in the first step of a cyclical procedure, we determine $\partial \boldsymbol{\omega}/\partial t$ from the transport equation of the vorticity, i.e., from (16), at every node point. In the next step we compute $\boldsymbol{\omega}^{t+\Delta t}$ from the following equation [1, 16, 33],

$$\boldsymbol{\omega}^{t+\Delta t} = \boldsymbol{\omega}^{t} + \Delta t\,\frac{\partial \boldsymbol{\omega}}{\partial t}, \tag{18}$$

where

$$\Delta t = \min\left(\frac{f h_i}{v_i}\right), \qquad i = x, y, z. \tag{19}$$

Here, v_i represents the velocity components and h_i is the distance of the node points from each other along x, y, and z coordinates. The value of parameter f is $0 < f \leqslant 1$ [33]. The higher the value of f the faster the iteration. However, if the value of f is increased, the probability of lack of convergence is greater. By solving (17) the value of $\mathbf{v}^{t+\Delta t}$ is given. Then, returning to (16), we continue the cycle until a required convergence criterion is satisfied. The velocity components in (17) were computed by an explicit scheme.

Two convergence criteria are defined: one for the vorticity, (20), and one for the velocity, (21) [19],

$$\max\left\{\frac{1}{N}\left(\sum_{n=1}^{N} \frac{\omega_i^{t+\Delta t} - \omega_i^{t}}{\bar{\omega}_i^{t}}\right)\right\} \leqslant \xi_1, \qquad i = x, y, z, \tag{20}$$

and

$$\frac{v_i^{t+\Delta t} - v_i^t}{\bar{v}_i^t} \leqslant \xi_2, \qquad i = x, y, z, \tag{21}$$

where N is the number of node points in the planes perpendicular to the x-axis, $\bar{\omega}_i^t$ is the average value of ω_i for all mesh points at time t, ξ_1 is the accuracy limit of the convergence criterion for the maximum change of the integrated relative vorticity at all points of the planes perpendicular to the x-axis for each coordinate during time interval Δt, $\bar{v}_i^t$ is the average value of v_i for all inner mesh points (mesh points within the surface of the bifurcation) at time t, and ξ_2 is the accuracy limit of the convergence criterion for the maximum change of the relative velocity at each inner node point for each coordinate during time interval Δt. Thus, convergence criteria have been defined in the case of vorticity concerning the planes perpendicular to axis x and in the case of velocity concerning each inner node point.

In order to solve the Navier–Stokes and Poisson equations, forward or central differences have been applied for the space coordinates and forward differences for time. It is well known that the forward differences provide greater stability, but the central differences supply faster convergency. Because in our case the central differences did not result in divergency for the final form of the model, we kept to the central space differences.

For the sake of faster convergence and greater stability slight underrelaxation was applied for the velocity components. That is, having determined $v_i^{t+\Delta t}$ from (17) in the course of an iteration, further on $^*v_i^{t+\Delta t}$ is applied, where

$$^*v_i^{t+\Delta t} = \alpha v_i^{t+\Delta t} + (1-\alpha)\, v_i^t, \qquad 0 < \alpha < 1. \tag{22}$$

Here α is the underrelaxation coefficient.

As an example the finite-difference representation of the derivatives $\partial u/\partial x$ and a $\partial^2 u/\partial x^2$ is:

$$\left.\frac{\partial u}{\partial x}\right)_{i,j,k}^{n} = \frac{u_{i+1,j,k}^n - u_{i-1,j,k}^n}{2h} \tag{23}$$

and

$$\left.\frac{\partial^2 u}{\partial x^2}\right)_{i,j,k}^{n} = \frac{u_{i+1,j,k}^n - 2u_{i,j,k}^n + u_{i-1,j,k}^n}{h^2}, \tag{24}$$

where u is the x component of the fluid velocity at the space points i, j, k and time coordinate n; and h is a constant grid distance.

The direction of marching when computing $\boldsymbol{\omega}$ and $\mathbf{v}$ from node point to node point was always reversed between two successive iterations in order to accelerate convergence and for more effective feedback of the boundary conditions [32].

It is impossible to build up the exact geometry of the bifurcation from cube-shaped elementary cells. On the other hand, in order to calculate particle trajectories and particle deposition, the most accurate possible description of the flow field is required in the vicinity of the surface of bifurcation. Irregular mesh points have been introduced to solve the problem. These mesh points are generated at the intersections of the wall of the bifurcation and the edges of the elementary cells. These intersections can be computed in an elementary mathematical way.

The fact that at the points next to the irregular mesh points the aforementioned central difference schemes are not applicable involves some difficulties because the mesh point distances in positive and negative directions are different. In these cases the model makes use of one of the following three methods:

(i) The use of first- and second-order Taylor series expansion for the difference scheme. If we keep to examples (23), (24) we obtain the formulae:

$$\left.\frac{\partial u}{\partial x}\right)_{i,j,k}^{n} = \frac{u_{i+1,j,k}^n + (\alpha^2 - 1)\, u_{i,j,k}^n - \alpha^2 u_{i-1,j,k}^n}{\alpha(\alpha+1)\, h_-} \tag{25}$$

and

$$\left.\frac{\partial^2 u}{\partial x^2}\right)_{i,j,k}^{n} = \frac{\begin{pmatrix} 2[u_{i+1,j,k}^n + \alpha^2 u_{i-1,j,k}^n - (\alpha^3+1)\, u_{i,j,k}^n \\ + (\alpha^3 - \alpha)(h_-)\, \partial u/\partial x)_{i,j,k}^n] \end{pmatrix}}{\alpha^2(\alpha+1)(h_-)^2}, \tag{26}$$

where $\alpha = h_+/h_-$. Here, h_+ and h_- are the distances of the node points in positive and negative directions, respectively.

(ii) The use of Taylor series expansion for the first derivatives only. For the second derivatives, the definition of the central difference scheme for the asymmetric interval is applied twice, so the following expression is derivable, keeping the example of $\partial^2 u/\partial x^2$:

$$\left.\frac{\partial^2 u}{\partial x^2}\right)_{i,j,k}^{n} = \frac{2}{h_-^2\, \alpha(\alpha+1)} \times [u_{i+1,j,k}^n - (\alpha+1)\, u_{i,j,k}^n + \alpha u_{i-1,j,k}^n]. \tag{27}$$

(iii) The calculation of $\boldsymbol{\omega}$ and $\mathbf{v}$ by interpolation using the adjoining six mesh points. As an example the velocity component in direction x at points i, j, k at time t is approximated as

$$\begin{aligned} u_{i,j,k}^n = \frac{1}{3}\Bigg[& u_{i-1,j,k}^n + (u_{i+1,j,k}^n - u_{i-1,j,k}^n)\frac{h_{x-}}{h_{x-}+h_{x+}} \\ & + u_{i,j-1,k}^n + (u_{i,j+1,k}^n - u_{i,j-1,k}^n)\frac{h_{y-}}{h_{y-}+h_{y+}} \\ & + u_{i,j,k-1}^n + (u_{i,j,k+1}^n + u_{i,j,k-1}^n)\frac{h_{z-}}{h_{z-}+h_{z+}}\Bigg], \end{aligned} \tag{28}$$

where h_{x-} and h_{x+} are the distances of the neighboring node points in positive and negative x directions. The meanings of h_{y-}, h_{y+}, h_{z-}, and h_{z+} are similar, but for the y and z directions.

Of the three methods, the first gives the most accurate approximation and the third is the least precise, supposing that in the course of the iterations the procedure does not result in divergence. Such a divergence may occur in the first and second cases if an inner node point is very near the surface, i.e., near to an irregular mesh point, so the central difference scheme is highly asymmetric. For the solution of this problem the computer program applies the following method: if the program arrives at an inner node point, which has at least one irregular mesh point neighbor, then the program calculates the distance of the nearest adjoining node point from the six. If it is greater than Q_1, then the program computes according to the first method. If it is between Q_1 and Q_2, where $Q_1 > Q_2$, then the program follows the second method. Finally, if it is less than Q_2, then the program calculates the components of $\boldsymbol{\omega}$ and $\mathbf{v}$ on the basis of the linear interpolation method. Here, Q_1 and Q_2 are empirical input parameters. Their values are between zero and one, supposing that the elementary cell distance is unity. During the running of the program it is worth following with attention the maximum and minimum values of the $\boldsymbol{\omega}$ and $\mathbf{v}$ components along the mesh points as well as their maximum changes during the iterations, together with the space coordinates of these node points. In such a way the lack of convergence or unrealistic $\boldsymbol{\omega}$ or $\mathbf{v}$ values can already be recognized at the beginning. If this happens, it is necessary to increase the values of Q_1 and/or Q_2. After these considerations let us see the initial and boundary conditions.

3.1. *Initial Conditions*

The model is worked out for both uniform and parabolic initial flow profile conditions. When constructing the flow field it is supposed that the flow rate is constant along the length of the system. The directions of initial flow in the parent and daughter branches are parallel with the axes of the branches. In the central part this direction is defined between the directions of the parent and daughter branches. The iteration procedure for solving the Navier–Stokes equations is not very sensitive to the initial conditions, in contrast to the boundary conditions. A more detailed description of the initial conditions is given in [6].

The absolute value of the velocity along the axes of branches is obtained by the average velocity characteristic of the branch and by the type of initial flow profile. The average velocity in the daughters (v_d) is

$$v_d = v_p \frac{R_p^2}{R_{dA}^2 + R_{dB}^2}, \tag{29}$$

where v_p is the average velocity in the parent branch. The absolute value of velocity in the central part along the $\overline{CD}$ section (see Fig. 1) is computed from the appropriate velocity values of the C and D points by linear interpolation. The model supposes that at point D the absolute velocity is v_d.

At points which do not lie on the axes the absolute value of velocity is computed on the basis of the presumed flow profile and the axial velocity values. In the case of the central part the calculation is quite circuitous because in this case it is necessary to determine at a given point the distance from not only the axis but from the surface as well, and the surface is not characterized by an analytical expression.

For a uniform initial velocity profile the velocity has to be kept to zero at the wall; otherwise an infinitely large velocity gradient would arise at the surface of the bifurcation. In this case a linearly varying velocity field is defined in radial directions in the surroundings of the wall, resulting in a truncated cone shape flow profile in the branches. The percentage of the branch radius where the velocity decreases in the vicinity of the walls in the case of uniform flow is an input parameter of the program.

The sum of the flow rates in the two daughters has to be equal with that in the parent branch. However, the ratio of the branch flow rates of the two daughters may be presented as an input parameter of the model. In this case the velocities given by (29) are modified with this input parameter.

3.2. *Boundary Conditions*

As the computation method is highly sensitive to the boundary conditions, these should be determined as accurately as possible. Let us see these conditions at the inlet (i), at the outlet (ii), and on the surface of the bifurcation (iii):

(i) Parabolic or uniform, stationary inlet boundary fluid flow is supposed in the model. In the case of uniform flow in the vicinity of the wall the velocity decreases linearly to zero, as has been discussed above. The vorticity is also kept constant in time at the inlet boundary.

(ii) At the outlet boundary it is presumed that both the velocity and the vorticity components have the same value as they have one layer before at the same cross-sectional point. If this identical cross-sectional point is not a node point then $\mathbf{v}$ and $\boldsymbol{\omega}$ are computed from the appropriate values of the surrounding points in the vicinity of the outlet boundary.

The value of flow rate at the outlet(s) has to be the same as at the inlet(s) because of the law of mass conservation. To check mass and momentum conservation, the computer program composes the integral of the axial velocity components at the outlet(s) and forms the quotient of this with the inlet flow rate(s). The result is a quite useful parameter (ε) for checking the fulfillment of the continuity equation. If this ε is not near unity, it means that the computation methods is not appropriate. The written computer program records and displays the value of ε during the iterations and multiplies the axial velocity values by ε at the outlet(s) after every second iteration.

It may occur that the flow is asymmetrical even if the geometry is symmetrical (e.g., if one of the daughters is evacuated more strongly than the other). Because in the applied numeric technique the pressure is not a variable, we describe this possible flow asymmetry with the proper definition of flow velocity at the ends of the daughter branches. Namely the ratio of flow rates at the ends of the daughter branches may be presented as an input parameter. In such cases the computed velocity values at each iteration at the outlets, for inhalation, are multiplied by a factor given by the assumptions that (i) the sum of the two flow rates in the daughters is equal to the inlet flow rate, (ii) the ratio of the two flow rates in the daughters is an input parameter. In case of exhalation the sum and the ratio of the two inlet flow rates are input parameters.

(iii) The third case—the boundary conditions on the surface of the bifurcation—is a somewhat more complex task. The main points of this are described below.

At the surface every component of the velocity is zero. As a consequence eddies cannot occur on the wall; i.e., the vorticity component perpendicular to the wall must be zero on the surface. For this, when calculating the vorticity on the wall in the case of each surficial mesh point it is worth introducing a new coordinate system where one of the axes is normal to the surface [33]. So the course of the computation is the following: (1) Let us define a right-handed rectangular Cartesian coordinate system x', y', z', where the axis x' is perpendicular to the wall and it is directed towards the inner side of the surface. Let the origin be the point P_0 where we intend to calculate $\boldsymbol{\omega}$. (2) Let us select two points P_1 and P_2 on the x' axis so that $\overline{P_0P_1} = \overline{P_1P_2}$, at the inner side of the bifurcation, in such a way that the distances of these points are close to the grid distance of the computer mesh. (3) Calculate the $\mathbf{v}(u, v, w)$ fluid velocity at P_1 and P_2. (4) In the knowledge of $\mathbf{v}$ determine $\mathbf{v}'(u', v', w')$ at P_1 and P_2. (5) Compute the vorticity $\boldsymbol{\omega}'(\alpha', \beta', \gamma')$ by means of a three-point forward difference approximation. (6) By the transformation of $\boldsymbol{\omega}'$ we obtain $\boldsymbol{\omega}$. A detailed description of these six procedures is given in [6].

In the model the surface of the bifurcation is regarded as a smooth surface and so, in the case of airways, the effect of cilia and flagella or the corrugated nature of the airway surfaces are not considered.

3.3. *Symmetry Planes*

The geometry of the bifurcation may have zero, one, or two symmetry planes. The geometric symmetry plane does not necessarily entail symmetric flow. Above Reynolds number ($\mathrm{Re} = vR/\nu$) 1150 it is generally not recommended that a flow symmetry plane be defined and thus decrease the degree of freedom of the flow because of the possible turbulence. Below $\mathrm{Re} = 1150$, if it is reasonable then it is permissible. Here we do not deal with the effect of the defined flow symmetry planes. Our conclusions on this are summarized in [6]. We would just mention that the defined symmetry planes really symmetrize the computed flow field. However, they also restrict the flow to some degree. Furthermore, it is supposed in every case that the occasional geometric symmetry planes of the bifurcation lie among the mesh points in the middle of the computer grid.

4. COMPUTATION OF PARTICLE TRAJECTORIES

Four different physical deposition mechanisms are taken into consideration by the model. These are: inertial impaction, gravitational sedimentation, Brownian diffusion, and interception.

4.1. *Inertial Impaction and Gravitational Sedimentation*

The motion equation of particles under the effect of inertial forces is described by the Basset–Boussinesq–Oseen equation [28]. If one incorporates the additional influence of the gravitational force and supposes that the particle density is much higher than that of the fluid, the motion equation can be described as

$$\left(1-\frac{\delta}{\sigma}\right) m \frac{d\mathbf{u}}{dt} = \left(1-\frac{\delta}{\sigma}\right) m\mathbf{g} + \frac{\mathbf{v}-\mathbf{u}}{B}, \qquad (30)$$

where m is the mass of the particle, $\mathbf{u}$ and $\mathbf{v}$ are the velocities of the particle and the fluid, respectively; $B = K_m/(3\pi\mu\, d_p)$ is the mechanical mobility of the particle, K_m is the Cunningham correction factor or slip factor, μ is the viscosity of the fluid, d_p is the particle diameter, σ and δ are the densities of the particle and the fluid, respectively, $\mathbf{g}$ is the gravitational acceleration, and t is the time.

The solution of (30) is

$$u_i^{t+\Delta t} = \kappa_i + (u_i^t - \kappa_i)\, e^{-\Delta t/\zeta}, \qquad i = x, y, z, \qquad (31)$$

where u_i^t and $u_i^{t+\Delta t}$ are the ith velocity components of the particle at time t and $t + \Delta t$, respectively; moreover,

$$\zeta = mB\left(1-\frac{\delta}{\sigma}\right) = \tau\left(1-\frac{\delta}{\sigma}\right) \qquad (32)$$

and

$$\kappa_i = \zeta g_i + v_i^t. \tag{33}$$

Here τ is the relaxation time of the particle, and g_i and v_i^t are the ith components of $\mathbf{g}$ and $\mathbf{v}$, respectively, at time t.

The translation of the particle during the time interval between t and $t+\Delta t$ is

$$l_i^{t+\Delta t} = l_i^t + \int_0^{\Delta t} [\kappa_i + (u_i^t - \kappa_i)\, e^{-t'/\zeta}]\, dt, \qquad i = x, y, z, \tag{34}$$

where l_i^t and $l_i^{t+\Delta t}$ are the ith space coordinates of the particle at time t and $t+\Delta t$, respectively, and t' is the time elapsed since t. From (34), the equation which describes the particle trajectories—supposing inertial impaction and sedimentation—is

$$l_i^{t+\Delta t} = l_i^t + \kappa_i\,\Delta t + (u_i^t - \kappa_i)\,\zeta(1 - e^{-\Delta t/\zeta}), \qquad i = x, y, z. \tag{35}$$

However, there are some difficulties in applying this method. Namely, if the step time, Δt, is much higher than the relaxation time of the particle, $\tau = mB$, then the velocity of the particle approaches the constant velocity of fluid, v_i^t, at the very beginning of Δt and then moves together with the fluid, independently of the diameter and density of the particle. As a consequence, the computed particle trajectories are virtually the streamlines of fluid and not the trajectories of the particles. We cannot choose an arbitrarily short interval Δt since the speed of the computers is limited. So with this method we can hardly calculate, say, particle deposition efficiencies for submicron particles where τ is quite short. This is the reason that the way in which [17] computed the deposition flux by impaction is likely to be ineffective for submicron particle sizes, as was mentioned in the Introduction. The opinion given in [25] is similar.

The following procedure can be used to solve the aforementioned problem. First, calculate by (35) the approximate translation $l_i^{t+\Delta t}$ of the particle during Δt at constant fluid velocity v_i^t. Then determine the fluid velocity at that point, ${}^*\mathbf{v}^{t+\Delta t}$. Finally, supposing constant fluid velocity gradient during Δt, compute $l_i^{t+\Delta t}$.

The motion equation, here, obtains the same form as (35), but instead of $\mathbf{v}$ we can now write:

$$\mathbf{v}_1 + \chi t \tag{36}$$

and

$$\chi = \frac{\mathbf{v}_2 - \mathbf{v}_1}{\Delta t}, \tag{37}$$

where $\mathbf{v}_1 \equiv \mathbf{v}^t$ and $\mathbf{v}_2 \equiv {}^*\mathbf{v}^{t+\Delta t}$. The solution of (36) is

$$u_i^{t+\Delta t} = b_i \zeta(\Delta t - \zeta) + a_i \zeta + (u_i^t - a_i \zeta + b_i \zeta^2)\, e^{-\Delta t/\zeta}, \qquad i = x, y, z, \tag{38}$$

and

$$l_i^{t+\Delta t} = l_i^t + \zeta[(\tfrac{1}{2} b_i\,\Delta t + a_i - b_i \zeta)\,\Delta t + (u_i^t - a_i \zeta + b_i \zeta^2) \times (1 - e^{-\Delta t/\zeta})], \qquad i = x, y, z, \tag{39}$$

where

$$a_i = g_i + \frac{v_i^t}{\zeta}, \qquad b_i = \frac{{}^*v_i^{t+\Delta t} - v_i^t}{\zeta\,\Delta t}. \tag{40}$$

The asterisk denotes that in this case the fluid velocity at $t+\Delta t$ is considered not in the final space, i.e., not at the point given by (39), but at the point given by (35). The velocity of the fluid at a fixed point ($\mathbf{v}^t$, ${}^*\mathbf{v}^{t+\Delta t}$, $\mathbf{v}^{t+\Delta t}$) is computed by interpolation from the velocity values in the mesh points around this space (see Section 4.4).

Figure 3 represents the difference between the results of the two aforementioned levels of approximation for computing the inertial impaction mechanism. The results of the method given by (30)–(35) are shown in Fig. 3a; the results of the method given by (30)–(40) are shown in Fig. 3b. It can be seen from Fig. 3 that if the fluid velocity is constant during Δt, then the calculated path of the particle is practically independent of the particle's diameter and follows the streamlines of the fluid (supposing that $\Delta t \gg \tau$). However, if in the neighborhood of l_i^t we know the velocity of the fluid, and we suppose that the velocity field is linear, and we then solve analytically the motion equation of particles, then, thanks to the analytical solution, we solve (35) for infinitesimally small Δt. Thus, the problem around $\Delta t \ll \tau$ automatically vanishes. We can say that the second method is not clearly numeric, it is numeric outside Δt and analytic within Δt. This analysis enables us to calculate well-separated, real particle trajectories (Fig. 3b).

4.2. *Brownian Motion*

The translation of particles by Brownian motion at times 0, Δt, $2\,\Delta t$, ... is treatable as a Markov process if $\Delta t \gg \tau$, where $\tau = mB$ is the relaxation time of the particles [15]. In this case, the probability distribution of the distances l_{Bi} travelled by the particle by Brownian motion along one coordinate during Δt is given by the Fokker–Planck equation and has the form

$$p(l_{Bi}, \Delta t) = \frac{1}{2\sqrt{\pi D^*\,\Delta t}}\, e^{-l_{Bi}^2/4D^*\Delta t}, \qquad i = x, y, z, \tag{41}$$

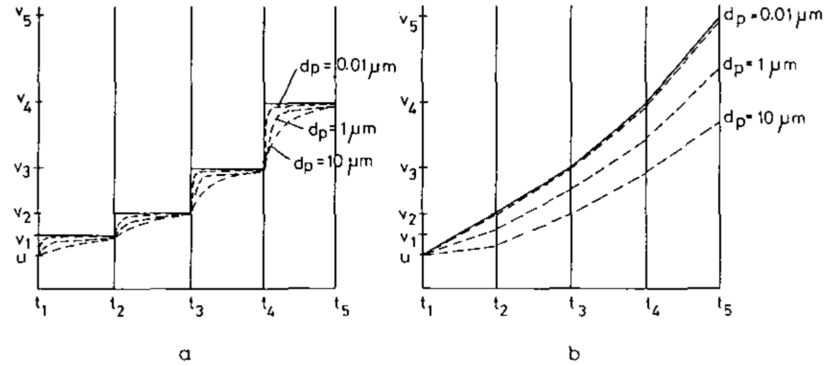

FIG. 3. Illustration of difference between results of two inertial impaction models: (a) v = const during Δt, (b) grad v = const during Δt.

where $-\infty < l_{Bi} < \infty$, $i = x, y, z$, and $D^* = kTB$ is the diffusion coefficient of the particle, k is the Boltzmann constant, T is the absolute temperature, and B is the mechanical mobility of the particle [18]. Values of l_{Bi} were selected from the normal distribution (41) by the Monte Carlo procedure published in [27].

If $\Delta t \ll \tau$, then the velocity of particles during Δt by Brownian motion along one coordinate, u_{Bi}, is selected from Maxwell's velocity distribution of the kinetic gas theory:

$$p(u_{Bi}) = \sqrt{m/2\pi kt}\, e^{-mu_{Bi}^2/(2kT)}, \qquad i = x, y, z, \tag{42}$$

where m is the mass of the particle, k is the Boltzmann constant, and T is the absolute temperature. Values of u_{Bi} ($-\infty < u_{Bi} < \infty$) were also selected by the Monte Carlo technique of [27]. The translation by Brownian motion was computed by the expression

$$l_{Bi} = u_{Bi}\, \Delta t, \qquad i = x, y, z. \tag{43}$$

The total displacement of the particle—by inertial impaction, gravitational sedimentation, and Brownian motion—along one coordinate, L_i, was computed as follows:

(a) If $\Delta t \gg \tau$, then L_i is the sum of the translations given by (39) and (41).

(b) If $\Delta t \ll \tau$, then L_i is the sum of the translations given by (39) and (43).

(c) If neither (a) nor (b) is fulfilled, i.e., when $0.2 < \Delta t/\tau < 5$, then the computer program decreases Δt in order to satisfy condition (b).

4.3. *Interception*

When modeling the deposition of spherical particles, the particles are considered to be deposited if their center of mass approaches the wall of the bifurcation to a distance of $d_p/2$. When the computer program examines whether or not the point where the particle resides has reached the wall of the bifurcation, then branch diameters are decreased by d_p. In the case of the central part, this procedure claims a comparatively lengthy computation.

4.4. *Special Problems*

In this section several additional parts of the model are discussed.

(1) The knowledge of fluid velocity, **v**, at an arbitrary point of the bifurcation is required both for (30)–(40) and for the computation of vorticity at the wall. In Section 4.3 the determination of fluid velocity at the node points was discussed by solving the Navier–Stokes and Poisson equations. Now, the determination of fluid velocity within an elementary cell is introduced.

If the whole elementary cell is within the bifurcation then the velocity is computed by linear interpolation from the velocities at the eight surrounding grid points. In this procedure, first we determine the velocities at the appropriate points of the twelve edges of the cell, then on the six faces, and finally at the point of interest within the elementary cell, for each velocity component by linear interpolation.

If the elementary cell touches or intersects the surface of the bifurcation, then the fluid velocity components, v_i, $i = x, y, z$, at the given point are computed from the appropriate velocity component values of the vertexes of the elementary cell that are within the bifurcation (inner grid points). The computation is

$$v_i = \frac{s^\phi}{n} \sum_{j=1}^{n} \frac{v_{ij}}{s_j^\phi}, \qquad i = x, y, z, \tag{44}$$

where v_{ij} is the ith velocity component in the jth vertex of that part of the elementary cell which is within the bifurcation, n is the number of inner grid points of the elementary cell, s is the distance of the given (inner) point from the surface of the bifurcation, s_j is the distance of the jth grid point from the wall of the bifurcation, and ϕ is a parameter specifying the type of interpolation. If $\phi = 1$ then linear interpolation is used. Because sometimes the form of the flow profile is far from linear it may be expedient to apply a ϕ value different from unity. According to the calculations—where the diameter of the parent airway was covered by 20 grid points—there is no significant difference in the particle deposition patterns at $\phi = 0.75$ and $\phi = 1.0$. The determination of the parameters s and s_j is a simple coordinate geometry task, which is quite lengthy in the case of the central part.

(2) It is assumed in the model that if the particles precisely follow the fluid streamlines then disregarding interception none of the particles are deposited. However, because the computer grid applied for computing the fluid velocity field is not infinitely fine, moreover, because the time interval for the computation of particle trajectories cannot be infinitesimally small, the deposition efficiency may differ from zero even if the effects of all the deposition mechanisms are neglected. To eliminate this unrealistic "deposition" effect one can define a numerical laminar boundary layer in the vicinity of the surface where the velocity component of the fluid perpendicular to the nearby wall is considered to be zero and where the absolute value of the velocity is unchanged, i.e., remains the same as it was without the application of the numerical boundary layer. For this computation the employment of a coordinate transformation is necessary, similar to that demonstrated for calculating the boundary conditions of $\boldsymbol{\omega}$ in Section 3.2. In the model the width of this numerical boundary layer (λ) is an input constant, where λ is much less than h, the grid distance.

The running time of the computer program is likely to increase significantly while computing the deposition efficiency if the number of steps of the particle in the numerical boundary layer is not limited, since the velocity of the fluid may be extremely low there. Having given an upper limit for this step number it is possible that the trajectory of a particle terminates within this boundary layer. If the computer grid is fine enough and if the step time of particles, Δt, is small enough, then the percentage of particles remaining in the boundary layer cannot be significant. For calculating the trajectories exempt from deposition mechanisms, i.e., for computing fluid streamlines—in order to determine the width of the boundary layer—it is worth writing a separate computer program in which the deposition mechanisms have no role. The width of the boundary layer is suitable if neither of the trajectories, free from deposition mechanisms, causes deposition and at the same time the layer is as thin as possible.

(3) The simulation of a particle trajectory is terminated if: (i) it crosses or touches the wall of the bifurcation; (ii) it leaves the system at the outlet with the fluid flow; (iii) the number of steps of the particle in the numerical boundary layer reaches a preset limit. In case (i) when the trajectory intersects the surface of the bifurcation, it is necessary to determine the exact location of this intersection by coordinate geometry calculations.

If a particle leaves the system from the inlet, the model does not take it into account unless a single trajectory of a particle is modeled.

(4) In possession of the method of computation of particle trajectories there is a possibility to calculate deposition efficiencies referred to the whole bifurcation or to different sections of it. In addition we can easily compute enhancement factors in the vicinity of the carinal ridge or bifurcation region. For these computations only the coordinates of the end points of the trajectories are to be recorded. The starting points of the trajectories are selected by a Monte Carlo method. Particles are selected at the inlet according to the probability distribution which corresponds to the inlet velocity distribution; this is parabolic for an inlet parabolic velocity profile and a truncated cone for an inlet uniform flow profile.

In consequence of the random selection scheme, the statistical uncertainty of the calculated deposition efficiencies decreases with increasing number of selected particles. The computer program calculates, in the case of any deposition efficiencies, the associated standard deviation, as well.

(5) The initial velocity of the selected particles at the inlet boundary is assumed to be equal to the fluid velocity.

Finally it is worth mentioning that at the inlet, at the outlet, and at the edges of the bifurcation different equations and conditions are usually required than at the four large parts of the geometry.

5. SAMPLE RESULTS

The main aim of this paper has been to describe the model. The structure of the computer program is described in [6]. Applications for determining airway deposition patterns together with the representations of the flow velocity fields will be detailed elsewhere: for inhalation in [7] and for exhalation in [8].

In this section, the results of some test calculations are presented where a few computed particle trajectories are displayed in a bifurcation which is characteristic of the upper airways in humans. The deposition of aerosol particles in single bifurcations was measured in [21–23], where the diameter of the parent airway was 0.5 cm and those of the daughters 0.4 cm at a wide range of branching angles. This system corresponds to generations 3–4 or 4–5 in Weibel's Model-A [37]. In the present calculations the

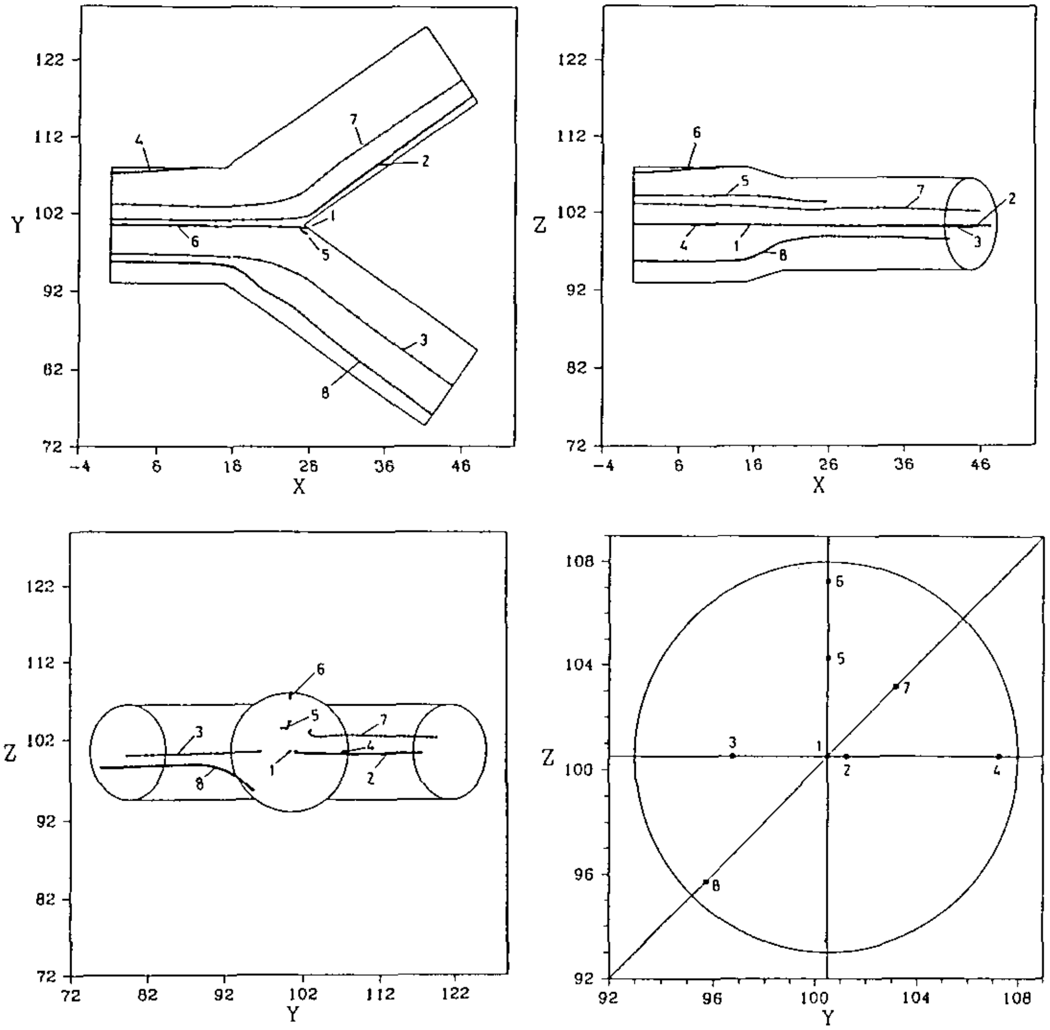

FIG. 4. Computed trajectories of eight particles, $d_p = 0.01$ μm, flow rate = 7.5 l/min. The figure also displays the initial coordinate points of the eight particles. The distance of these points from the origin (i.e., point 1) are: point 2, $0.1R_p$; points 3, 5, and 7, $0.5R_p$; points 4, 6, and 8, $0.9R_p$ (R_p = parent airway radius).

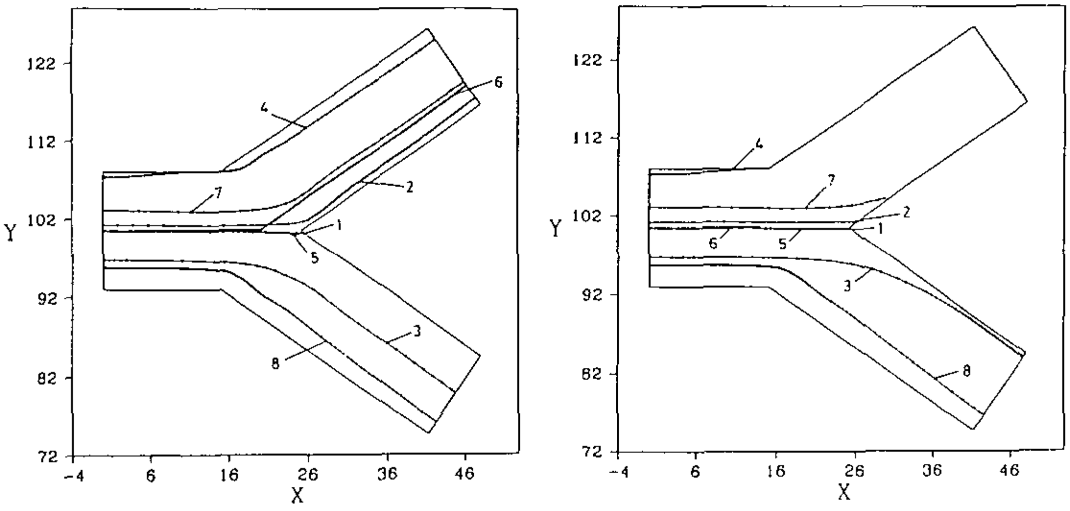

FIG. 5. Computed trajectories of eight particles, $d_p = 0.5$ μm (left), and $d_p = 10.0$ μm (right), flow rate = 7.5 l/min, only X–Y projection.

other parameters of the system are the following: both branching angles are 35°, the axes of the branches lie in a horizontal plane, the length of the parent branch is 0.5 cm, the lengths of the daughters are 1.0 cm, the central part is narrow, see (4). The number of node points of the computer grid is about 31,000. The diameter of the parent airway contains 20 mesh points. The two symmetry planes of the bifurcation lie between the mesh points in the middle. The flow rate (inhalation) in the parent airway is 7.5 l/min in the case of Figs. 4–5, but computations were also made at a flow rate 1.25 l/min. If it is supposed that the bifurcation represents generations 3–4 (Weibel's Model-A), these flow rates yield 60 l/min and 10 l/min in the trachea, which rates correspond to normal working and resting conditions, respectively. The related average air velocities in the parent branch are 636.6 cm/s and 106.1 cm/s, with Reynolds numbers of 1066 and 178, respectively. The inlet boundary flow profile is parabolic. The value of f in (19) is 0.7, and the underrelaxation coefficient in (22) varies between 0.6 and 1.0. The *defined convergence criteria values,* ξ_1 *and* ξ_2 *in (20) and* (21), were between 0.1 and 0.01. In Section 3, three methods were mentioned for determining the velocity and vorticity vectors adjacent to the irregular mesh points. Empirical input parameters Q_1 and Q_2 were introduced to select one of the three methods. The values of Q_1 and Q_2 are 0.4 and 0.2, respectively. (It is worth mentioning that for exhalation, where the maximum of grad $\mathbf{v}$ is significantly less, these values are 0.1 and 0.05). The value of parameter ε, which was defined in Section 3.2 when discussing the outlet boundary conditions for the examination of the fulfillment of mass conservation, is between 0.996 and 1.004 in the case of each of the iterations. In the same section, for the computation of $\boldsymbol{\omega}$ a $\overline{P_0P_1} = \overline{P_1P_2}$ distance, normal to the surface, was introduced, marked—in grid distance units—by q. According to some test calculations in the case of a computer grid where the parent branch includes 20 node points, there is no significant change in the calculated velocity field if parameter q varies between 0.7 and 1.3. So $q = 1.0$ is applied for the computations of the presented figures. The value of parameter ϕ in (44) is 1.0, and λ, the width of the numerical boundary layer, is less than 5 μm.

In Figs. 4 and 5 the trajectories of eight spherical, unit density particles are presented. The initial positions of the particles are displayed in Fig. 4. One particle, identified by 1, starts from the axis of the parent branch, i.e., from the origin of the figure. The others from the axes y, or z, or from the straight line $y = z$. The distances of these points from the origin are 10, 50, or 90% of the radius of the parent branch.

Figures 4, 5a, and 5b present the trajectories of $d_p = 0.01$ μm, $d_p = 0.5$ μm, and $d_p = 10$ μm diameter particles, respectively, at high flow rate (7.5 l/min in the parent airway). The step time at the generation of the trajectories is $\Delta t = 5 \times 10^{-5}$ s, in every case. The displayed particle trajectories in Figs. 4 and 5 contain both the computed residence points of the particle at the ends of each of the time intervals Δt (marked with dots) and a fitted curve on the dots. In such a way the speed of the particles is also represented since the distance between two neighboring dots is always taken during $\Delta t = 5 \times 10^{-5}$ s. Comparing the figures we can see that the deposition probability is the highest at $d_p = 10$ μm, where only two of the eight particles leave the system, and it is the smallest at $d_p = 0.5$ μm, where only two particles are deposited. In the case of large particles, impaction is the dominant mechanism; for very small particles, it is diffusion. Both mechanisms result in some deviation from the fluid streamlines and so may cause deposition. The $x - y$ panels of the figures clearly present the effect of inertial impaction (see curve Nos. 3, 7, and 2). In Fig. 5, right panel, curve No. 3 shows much stronger inertial impactional effect than curve No. 8 in the same panel, both for the same particle size. The reason is in the difference between the particle velocities. A parameter which characterizes the effect of inertial impaction is the Stokes number, $\mathrm{St} = u\tau/R = \sigma\, d_p^2 u K_m/(18\mu R)$ *(the meanings of the symbols are given in* Section 4.1). The higher the particle velocity, the greater the influence of inertial impaction. The values of St are: 1.5×10^{-5}, 2.7×10^{-3}, and 0.80 for Figs. 4, 5a, and 5b, respectively.

Similar computations have also been made at one-sixth the flow rate (1.25 l/min). In this case the effect of inertial impaction is significantly less than it was at high flow rate. (The appropriate values of St are 2.6×10^{-6}, 4.5×10^{-4}, and 0.13 for $d_p = 0.01$ μm, $d_p = 0.5$ μm, and $d_p = 10$ μm diameter particles.) Here only three particles deposit at each of the three figures, and these are the particles which start from the xz symmetry plane of the bifurcation (curve Nos. 1, 5, and 6).

6. SUMMARY AND CONCLUSION

Earlier we worked out analytical solutions—[3–5, 9]—for determining aerosol particle deposition in curved and bifurcating tubes both for spherical and fibrous particles. Here a numerical solution has been presented for computing particle trajectories and particle deposition patterns in real bifurcation geometry with both wide and narrow central regions. The fluid velocity field is computed by solving the Navier–Stokes and Poisson equations, and the *simultaneous effects of inertial impaction, gravitational* sedimentation, Brownian motion, and interception mechanisms are considered. Both the orientation of the branches to gravity and the direction of flow in the bifurcation are optional. In order to calculate deposition patterns or efficiencies the initial coordinates of the selected particles are determined by a Monte Carlo selection technique, similarly to the computation of particle diffusion.

With the help of this model there is a possibility to compute local deposition patterns in bifurcating tubes. One important application of the model may be in examining aerosol particle behavior in bifurcating human airways. In the currently used aerosol deposition lung models the bifurcations are substituted by simple bent tubes, the air velocity fields are highly simplified and idealized; moreover, the different deposition mechanisms are treated independently, and the same model is applied for inhalation and exhalation. In addition the simple bent tube model does not say anything about the distribution of deposition along the length or surface of a bifurcation. At the same time the potential adverse health effects of inhaled particles mainly depend on the local doses and not on the average values. So the current model may have significance from the dosimetric aspect as well: by defining enhancement factors, more realistic dose calculations can be performed than by assuming homogeneous dose distribution.

The model presented here makes it comparatively easy to examine the influence of one bifurcation on another: the computed fluid and particle velocity distributions at the outlet boundary of the first bifurcation have to be applied as inlet boundary conditions on the second bifurcation.

A useful feature of this method is that it can be developed relatively easily and, in principle, optional physical effects can be incorporated into the model.

It is indicated in the previous section that applications of the model are due to be published elsewhere. However, to demonstrate the validity of the model it is mentioned here that the deposition efficiency and distribution were examined as a function of parameters affecting the particle deposition pattern in airways, such as particle size and density, flow rate, inlet flow profile, airway diameter, and length, branching, and gravity angles, width of the bifurcation zone, and asymmetry of airway branching. The model has been tested by comparison with experimental data [21–23]. Our theoretical results [7, 8] show excellent agreement with the experimental findings.

REFERENCES

1. D. A. Anderson, J. C. Tannehill, and R. H. Fletcher, *Computational Fluid Mechanics and Heat Transfer* (Hemisphere, Washington, DC, 1984).
2. K. Aziz and J. D. Hellums, *Phys. Fluids* **10**, 314 (1967).
3. I. Balásházy, W. Hofmann, and T. B. Martonen, *Aerosol Sci. Technol.* **13**, 20 (1990).
4. I. Balásházy, W. Hofmann, and T. B. Martonen, *Aerosol Sci. Technol.* **13**, 308 (1990).
5. I. Balásházy, T. B. Martonen, and W. Hofmann, *J. Aerosol Med.* **3**, 243 (1990).
6. I. Balásházy, KFKI Report 1991-27/K, Budapest, Hungary, 1991.
7. I. Balásházy and W. Hofmann, *J. Aerosol Sci.* **24**, 745 (1993).
8. I. Balásházy and W. Hofmann, *J. Aerosol Sci.* **24**, 773 (1993).
9. I. Balásházy, W. Hofmann, and T. B. Martonen, *J. Aerosol Sci.* **22**, 15 (1991).
10. K. A. Bell and S. K. Friendlander, *Staub-Reinhalt. Luft.* **33**, 178 (1973).
11. K. A. Bell, in *Recent Developments in Aerosol Science* (Wiley, New York, 1978), p. 97.
12. R. W. Davis, E. F. Moore, and L. P. Purtell, *Phys. Fluids* **27**, 46 (1984).
13. S. C. R. Dennis, D. B. Ingham, and R. N. Cook, *J. Comput. Phys.* **33**, 325 (1979).
14. G. A. Ferron, A. Hillebrecht, J. Peter, E. Priesack, M. Thoma, I. Künzer, R. Mederer, and U. G. Klump, *J. Aerosol Sci.* **22**, S809 (1991).
15. N. A. Fuchs, *The Mechanics of Aerosols* (Pergamon, Oxford, 1964).
16. K. Goda, *J. Comput. Phys.* **30**, 76 (1979).
17. L. Gradon and D. Orlicki, *J. Aerosol Sci.* **21**, 3 (1990).
18. A. Hautojärvi, M. Hautala, and T. Raunemaa, *J. Aerosol Sci.* **14**, 507 (1983).
19. C. Hirsch, *Numerical Computation of Internal and External Flows, Vols. I, II* (Wiley, New York, 1988).
20. M. Y. Jaffrin and T. V. Hennessey, *Bull. Physio-Pathol. Respir.* **8**, 375 (1972).
21. J. R. Johnston, K. D. Isles, and D. C. F. Muir, in *Inhaled Particles IV*, edited by W. H. Walton (Pergamon, Oxford, 1977), p. 61.
22. C. S. Kim and A. J. Iglesias, *J. Aerosol Med.* **2**, 1 (1989).
23. C. S. Kim, A. J. Iglesias, and L. Garcia, *J. Aerosol Med.* **2**, 15 (1989).
24. N. I. Kolev, *Transiente Zweiphasenströmung* (Springer-Verlag, Berlin, 1986).
25. A. G. Konstandopoulos, *J. Aerosol Sci.* **21**, 983 (1990).
26. J. W. Lee and J. H. Goo, *J. Aerosol Med.* **4**, S1, 33 (1991).
27. E. J. McGrath and D. C. Irving, Oak Ridge National Laboratory Report ORNL-RSIC-38, Oak Ridge, TN, 1975.
28. A. R. Morrison, Jr., *J. Aerosol Sci.* **5**, 241 (1974).
29. T. J. Pedley, *Annu. Rev. Fluid Mech.* **9**, 229 (1977).
30. W. E. Pracht and J. U. Brackbill, Los Alamos Scientific Laboratory Reports. LA-6342, UC-32, and UC-34, August 1976.
31. S. M. Richardson and A. R. H. Cornish, *J. Fluid Mech.* **82**, 2, 309 (1977).
32. R. D. Richtmyer, *Difference Methods for Initial-Value Problems* (Wiley, New York, 1967).
33. P. J. Roache, *Computational Fluid Dynamics* (Hermosa, Albuquerque, NM, 1976).
34. R. C. Schroter and M. F. Sudlow, *Respir. Physiol.* **7**, 341 (1976).
35. F. T. Smith, *Proc. R. Soc. London Ser. A* (1976).
36. N. Takemitsu, *J. Comput. Phys.* **61**, 499 (1985).
37. E. R. Weibel, *Morphometry of the Human Lung* (Springer-Verlag, Berlin, 1963).